# Internal solitary wave generation by tidal flow over topography

**R. Grimshaw**[1] AND **K. R. Helfrich**[2]†

[1]Department of Mathematics, University College London, WC1E 6BT, UK
[2]Department of Physical Oceanography, Woods Hole Oceanographic Institution, Woods Hole, MA USA

Oceanic internal solitary waves are typically generated by barotropic tidal flow over localised topography. Wave generation can be characterised by the Froude number $F = U/c_0$, where $U$ is the tidal flow amplitude and $c_0$ is the intrinsic linear long wave phase speed, that is the speed in the absence of the tidal current. For steady tidal flow in the resonant regime, $\Delta_m < F - 1 < \Delta_M$, a theory based on the forced Korteweg-de Vries equation shows that upstream and downstream propagating undular bores are produced. The bandwidth limits $\Delta_{m,M}$ depend on the height (or depth) of the topographic forcing term, which can be either positive or negative depending on whether the topography is equivalent to a hole or a sill. Here the wave generation process is studied numerically using a forced Korteweg-de Vries equation model with time-dependent Froude number, $F(t)$, representative of realistic tidal flow. The response depends on $\Delta_{max} = F_{max} - 1$, where $F_{max}$ is the maximum of $F(t)$ over half of a tidal cycle. When $\Delta_{max} < \Delta_m$ the flow is always subcritical and internal solitary waves appear after release of the downstream disturbance. When $\Delta_m < \Delta_{max} < \Delta_M$ the flow reaches criticality at its peak, producing upstream and downstream undular bores that are released as the tide slackens. When $\Delta_{max} > \Delta_M$ the tidal flow goes through the resonant regime twice, producing undular bores with each passage. The numerical simulations are for both symmetrical topography, and for asymmetric topography representative of Stellwagen Bank and Knight Inlet.

† Email address for correspondence: rgrimshaw@ucl.ac.uk

## 1. Introduction

Although there have been many studies of the propagation of oceanic internal solitary waves (ISW), see for instance the recent reviews by **????**, the generation process has been relatively less well studied. Nevertheless the essential characteristics are known, from theory, observations and numerical simulations. In the context of this work, we note especially the many studies in Knight Inlet and other fjords (**???????**) over Stellwagen bank in Massachussets Bay (**?????**) and in the South China Sea (**??????????????**). From these and many other studies we infer that in shallow water, there are essentially just two mechanisms, each involving the interaction of the barotropic tide with a localised topographic feature. One is the generation of an internal tide which steepens as it propagates away from the forcing site, and then generates ISW; this is usually associated with low sub-critical Froude numbers, $F = U/c_0 < 1$ where $U$ is the tidal velocity and $c_0$ is the relevant intrinsic linear long wave speed. This scenario can be modelled with the Korteweg-de Vries (KdV) equation, in which the initial condition are the essentially linear waves formed by the interaction of the tide with the topography. The other is the generation of an upstream propagating undular bore composed of ISW, often developing from an upstream hydraulic jump; this is usually associated with transcritical (or resonant) flow, $F \sim 1$. This scenario can be modelled with the forced Korteweg-de Vries (fKdV) equation, in which the forcing term is provided by the interaction of the tide with a localised topographic feature. There are of course many features specific to each particular location, but these two scenarios would seem to cover most observations when a barotropic tide interacts with a *localised* topographic feature. There is a third mechanism which operates when a barotropic tide interacts with the topography, generating strong internal tidal beams from a critical point in the slope, which in turn interact with the pycnocline to form ISW (**??**). This case being more associated with deep water scenarios is not our concern here.

However, these fKdV scenarios are usually based on a constant fixed Froude number $F$ whereas in practice this varies, albeit slowly, as the tide varies over a tidal period. Although one might nevertheless expect that each of these scenarios will hold locally in time, as the generation timescale can be expected to be significantly shorter than the tidal period, it is useful to examine how these models behave when the tide, and hence the Froude number $F$ is allowed to vary slowly in time. This is the purpose of the present paper, where we examine the fKdV model with a time-dependent Froude number, and so with time-dependent forcing. Our aim is to demonstrate within the framework of this model that the generation of large-amplitude ISW occurs near the localised topography when the tide enters the transcritical regime, and that these waves are released upstream as the tide slackens. Surprisingly, there seem to have been relatively few such studies of a time-dependent fKdV equation, although we note the work of **?** who reported some numerical simulations in which the $F$ was varied in the transcritical range, but the topographic forcing was kept constant. Pertinently **??** made comparisons between the fKdV model and numerical simulations of the full nonlinear equation for time-dependent flow over localised topography resembling Knight Inlet. Although they found that internal wave breaking near the topographic forcing region prevented direct quantitative comparisons with the fKdV model, they did conclude that the upstream propagating ISW were generated when the tidal flow is in the transcritical regime.

In section 2 we present a summary of the fKdV equation and the relevant solution scenarios when $F$ is a constant, and speculate how these scenarios can be used to describe the case when $F$ varies. Then in section 3 we present some numerical simulations when $F$ is allowed to vary slowly in time using parameters derived from a two-layer fluid model

and a localised symmetric topographic forcing. In section 4 we extend these simulations to representations of some well-known actual observed cases of ISW generation characterised by asymmetric topography. We conclude in section 5.

## 2. Forced Korteweg-de Vries equation

The asymptotic derivation of the fKdV equation for internal waves was first given by **??**, and its relevant solutions can be found there, and in many other works, for a recent review see **?**. The outcome is briefly summarised here. At the leading order we get linear long wave theory,

$$\zeta \sim A(x,t)\phi(z) + \cdots , \tag{2.1}$$

Here $\zeta$ is the vertical particle displacement relative to the basic state, defined by the background density field $\rho_0(z)$ and background current $u_0(z)$. The modal function $\phi(z)$ satisfies the system

$$\{\rho_0(c-u_0)^2\phi_z\}_z + \rho_0 N^2\phi = 0 , \quad \rho_0 N^2 = -g\rho_{0z} , \qquad \text{for} \quad -h < z < 0 , \tag{2.2}$$

$$\phi = 0 \quad \text{at} \quad z = -h , \quad (c-u_0)^2\phi_z = g\phi \quad \text{at} \quad z = 0 , \tag{2.3}$$

In general this has an infinite set of solutions for $\phi(z)$ and the linear long wave speed $c$, but for oceanic internal waves it is customary to examine only mode one which has the fastest internal wave speed (formally the lowest mode zero is the surface wave mode with speed $c \approx (gh)^{1/2}$ in the absence of background current). As usual we normalise $\phi$ so that $\phi(z_m) = 1$ where $z = z_m$ is the location of the extremum of $\phi$. Then the fKdV equation is, written in the reference frame of the topography, given by $z = -h + b(x)$,

$$-A_t - cA_x + \mu AA_x + \delta A_{xxx} + \gamma b_x(x) = 0 . \tag{2.4}$$

$$I\mu = 3\int_{-h}^{0} \rho_0(c-u_0)^2\phi_z^3 \, dz ,$$

$$I\delta = \int_{-h}^{0} \rho_0(c-u_0)^2\phi^2 \, dz ,$$

$$I\gamma = \rho_0 u_0(u_0 - c)\phi_z , \quad \text{at} \quad z = -h , \tag{2.5}$$

$$I = 2\int_{-h}^{0} \rho_0(u_0 - c)\phi_z^2 \, dz .$$

At resonance (that is, at criticality, see below in the next paragraph), $c = \Delta \approx 0$ and this reduces to the more familiar form,

$$-A_t - \Delta A_x + \mu_0 AA_x + \delta_0 A_{xxx} + \gamma_0 b_x(x) = 0 . \tag{2.6}$$

$$I_0\mu_0 = 3\int_{-h}^{0} \rho_0 u_0^2\phi_z^3 \, dz ,$$

$$I_0\delta_0 = \int_{-h}^{0} \rho_0 u_0^2\phi^2 \, dz ,$$

$$I_0\gamma_0 = \rho_0 u_0^2\phi_z , \quad \text{at} \quad z = -h , \tag{2.7}$$

$$I_0 = 2\int_{-h}^{0} \rho_0 u_0\phi_z^2 \, dz .$$

Here the modal function $\phi$ is evaluated at $c = 0$, but $c = \Delta$ is retained in the leading order terms to ensure that all terms remain in balance.

It is now useful to consider the special case when $u_0 = U = \text{constant}$. Then the speed $c = U - c_0$ where $c_0$ is the intrinsic linear long wave speed, that is the speed in the absence of a background flow. In that case $c = c_0(F - 1)$ where $F = U/c_0$ is the Froude number, and the modal equation becomes

$$c_0^2 \{\rho_0 \phi_z\}_z + \rho_0 N^2 \phi = 0, \quad \text{for} \quad -h < z < 0, \tag{2.8}$$

$$\phi = 0 \quad \text{at} \quad z = -h, \quad c_0^2 \phi_z = g\phi \quad \text{at} \quad z = 0, \tag{2.9}$$

The coefficients become, to leading order

$$I_0 \mu_0 = 3 \int_{-h}^{0} \rho_0 c_0^2 \phi_z^3 \, dz,$$

$$I_0 \delta_0 = \int_{-h}^{0} \rho_0 c_0^2 \phi^2 \, dz,$$

$$I_0 \gamma_0 = \rho_0 c_0 U \phi_z, \quad \text{at} \quad z = -h, \tag{2.10}$$

$$I_0 = 2 \int_{-h}^{0} \rho_0 c_0 \phi_z^2 \, dz.$$

When $U$ varies temporally, the coefficients $\mu_0, \delta_0$ remain constant, and in the fKdV equation (2.4), only the coefficients $c = U - c_0 = c_0(F - 1)$ and $\gamma_0$ vary, where

$$\gamma_0 = F\sigma_0, \quad I_0 \sigma_0 = \rho_0 c_0^2 \phi_z, \quad \text{at} \quad z = -h. \tag{2.11}$$

Next, rescale by

$$\tilde{A} = \frac{\mu_0 A}{6c_0}, \quad \tilde{\Delta} = \frac{c}{c_0}, \quad \tilde{t} = \{\frac{c_0^3}{\delta_0}\}^{1/2} t, \quad \tilde{x} = \{\frac{c_0}{\delta_0}\}^{1/2} x, \quad \tilde{b} = \frac{\sigma_0 \mu_0 b}{6c_0^2}, \tag{2.12}$$

so that (2.6) adopts the non-dimensional canonical form, after removing the tilde superscript,

$$-A_t - \Delta A_x + 6AA_x + A_{xxx} + Fb_x(x) = 0, \quad F = 1 + \Delta. \tag{2.13}$$

For mode one, since $\phi$ has a positive extremum, $\sigma_0 > 0$ and so the forcing is positive when $\mu_0 b > 0$ but negative when $\mu_0 b < 0$. In particular, flow of a two-layer fluid with a near-surface pycnocline over a sill is equivalent to negative forcing.

The solutions fall into three categories, see **??**, subcritical $\Delta < \Delta_m < 0$, transcritical $\Delta_m < \Delta < \Delta_M$ and supercritical $\Delta > \Delta_M > 0$. Here the regime boundaries $\Delta_{m,M}$ depend on the forcing. For the asymptotic limit of broad forcing, also known as the hydraulic limit,

$$\Delta_{M,m} = \pm\{12F|b_M|\}^{1/2}, \tag{2.14}$$

where $b_M$ is the maximum obstacle displacement and is positive when $b > 0$, or negative when $b < 0$. In the usual fKdV limit, we can set $F \approx 1$ here, but using the relation $F = 1 + \Delta$ a refinement is

$$\Delta_{M,m} = 6|b_M| \pm \{12|b_M| + 36b_M^2\}^{1/2}. \tag{2.15}$$

Thus the supercritical boundary is increased and the subcritical boundary is decreased.

The subcritical and supercritical regimes are essentially linear and near the obstacle in a steady state. They are given by the approximate expressions valid for large $|\Delta|$ and as $t \to \infty$,

$$A \sim \frac{Fb}{\Delta} + H(x)\frac{Fb_m}{|\Delta|^{1/2}} \sin\left(|\Delta|^{1/2} x\right), \quad \Delta \to -\infty, \quad b_m = \int_{-\infty}^{\infty} b(x) \, dx, \tag{2.16}$$

$$A \sim \frac{Fb}{\Delta}, \quad \Delta \to \infty. \tag{2.17}$$

Here $H(x)$ is the Heaviside function. The subcritical solution (2.16) is obtained by solving the steady-state linearized form of the fKdV equation (2.13), while for the supercritcal solution (2.17) the exponential decay away from the localised forcing is omitted as this occurs on a very short length scale $\Delta^{-1/2}$. Note that in (2.16) $\Delta = F - 1$ is bounded from below by $F = 0$. Close to the regime boundaries, the nonlinear terms provide corrections, and in particular the sinusoidal lee waves in (2.16) are replaced with cnoidal waves. In the transcritical regime, for positive forcing, the solution consists of a steady hydraulic solution over the obstacle, terminating with an upstream elevation resolved by an upstream propagating undular bore, and a downstream depression terminated by a downstream propagating undular bore. Figure 1 shows a numerical solution of (2.13) with $b_M = 0.01$ and $\Delta = 0$. The constant forcing is started impulsively with $A(x,0) = 0$. Details of the numerical scheme are discussed below. As $\Delta$ increases towards $\Delta_M$ the upstream undular bore resembles more a sequence of solitary waves, and the downstream undular bore weakens, and as $\Delta$ decreases towards $\Delta_m$ the upstream undular bore weakens, and the downstream undular bore intensifies. For negative forcing, the same scenario occurs upstream and downstream, but the flow over the obstacle remains unsteady, and there is some modulation of the upstream and downstream undular bores as illustrated in Figure 2 for $b_M = -0.01$ and constant $\Delta = 0$.

## 3. Generation of internal undular bores by tidal interaction with symmetric topography

The generation of internal undular bores by tidal flow can now be modelled by supposing that $\Delta$ varies slowly with time. Suppose for instance that $\Delta$ increases from a large negative value ( formally $\Delta = -1$ where $F = 0$) to a maximum value of $\Delta_{max}$ and then decreases back again, modelling the onset of an increasing tidal current followed by a decreasing tidal current, both in the same positive $x$-direction. Then three scenarios can be identified.

(1) If $\Delta_{max} < \Delta_m$ then the flow is always subcritical. On the increasing tide lee waves are generated, which reach a maximum amplitude at $\Delta_{max}$. These waves cannot be maintained as $\Delta$ decreases on the decreasing tide, and so propagate over the obstacle and then upstream.

(2) If $\Delta_m < \Delta_{max} < \Delta_M$ the flow reaches criticality at its peak. During the peak period, internal undular bores propagate slowly both upstream and downstream. But as the tide recedes, the upstream and downstream undular bores propagate back upstream. This could be identified as the Maxworthy mechanism (**?**). In his laboratory experiment a large depression formed in the lee of the obstacle when the tidal flow reached criticality. As the tidal flow slackened the depression moved back upstream and evolved into several internal solitary waves.

(3) If $\Delta_{max} > \Delta_M$ the flow passes through the transcritical regime as the tide develops, passes into the supercritical regime at the peak tide, and then again passes through the transcritical regime as it weakens. In this case the strongest internal undular bores are generated in the middle stage as the tide strengthens and then again at the middle stage as the tide weakens. On the growing tide these undular bores are swept downstream as the peak tide is approached, but propagate back upstream as the tide weakens.

We next present some numerical solutions for time-dependent forcing $F(t)$. We consider

the specific case of sinusoidal barotropic tidal flow

$$\Delta = F_{max} \sin(\omega t) - 1, \tag{3.1}$$

over half of a tidal cycle, $0 \le t \le \pi/\omega$, where $\omega$ is the tidal frequency. This forcing may pass through the resonant regime on both the acceleration and deceleration phase, may reside in the resonant regime for an extended period, or may not be large enough to enter the resonant regime, depending on $\Delta_{max} = F_{max} - 1$ and $\Delta_{M,m}$ from (2.15) (or (2.14)). Figures 3 and Figure 4 show, respectively, an example of these three possibilities for $b_M = 0.03$ and the resonant band $1 + \Delta_{M,m}$ from (2.15).

Using (2.12) the scaled frequency $\tilde{\omega} = \omega(\delta/c_0^3)^{1/2}$ (re-introducing the tildes). With the (dimensional) topography

$$b(x) = b_M s(x),$$

where $s(x)$ is a shape function with $\max(s) = 1$ and $b_M$ is the amplitude, the forcing term in (2.13) becomes

$$F(\tilde{t})\tilde{b}_{\tilde{x}} = F(\tilde{t})\tilde{b}_M s_{\tilde{x}}, \quad \text{where} \quad \tilde{b}_M = \frac{\sigma_0 \mu_0 b_M}{6c_0^2}.$$

Estimates for the non-dimensional parameters $\tilde{\omega}$ and $\tilde{b}_M$ are found by considering a Boussinesq, two-layered stratification with layer depths $h_i$ and densities $\rho_i$ in each layer. Here $i = 1, 2$ indicates the upper and lower layers, respectively. The coefficients (2.10) and (2.11) become

$$\mu_0 = \frac{3}{2}c_0\frac{h_1 - h_2}{h_1 h_2}, \quad \delta_0 = \frac{c_0}{6}h_1 h_2, \quad \sigma_0 = \frac{c_0}{2}\frac{h_1}{h_1 + h_2}, \quad \text{and} \quad c_0 = \left(g'\frac{h_1 h_2}{h_1 + h_2}\right)^{1/2}, \tag{3.2}$$

with $g' = g(\rho_2 - \rho_1)/\rho_1$. Conditions representative of the coastal ocean are total depth $H = h_1 + h_2 = 100 - 300$ m, $0.1 < h_1/H < 0.5$, $|b_M|/H \lesssim 0.2$, $g' = 0.01 - 0.02$ m s$^{-2}$, and semi-diurnal tidal frequency $\omega = 1.41 \times 10^{-4}$ s$^{-1}$. From (2.12), the normalizing length scale $(\delta_0/c_0)^{1/2} = 10 - 60\,m$ and time scale $(\delta_0/c_0^3)^{1/2} = 30 - 70\,s$. These parameter ranges give $|\tilde{b}_M| \lesssim 0.05$ and $\tilde{T} = 2\pi/\tilde{\omega} = 700 - 1500$. The topographic shape is taken to be a Gaussian

$$s(\tilde{x}) = e^{-(\tilde{x}/\tilde{w}_b)^2}, \tag{3.3}$$

with scaled width $\tilde{w}_b = w_b(c_0/\delta_0)^{1/2} = 25 - 100$ for $w_b/H \approx 5 - 10$.

Numerical solutions of (2.13) were obtained with a Fourier pseudo-spectral discretization in $x$. The nonlinear term was dealiased using the 2/3-rule truncation. Temporal integration employed a third-order, low-storage Runge-Kutta scheme (**?**). The barotropic forcing was given by (3.1) for $t \le T/2$ and the topographic shape by (3.3). The maximum forcing $F_{max} = 0.5 - 2$, $T = 600 - 1400$, $|b_M| \le 0.06$ and $w_b = 25$ and $75$ (after again dropping the tildes). The scheme is periodic in $x$, although the domain size was always taken large enough to avoid end effects. A typical domain had a length of 1500 and used 3072 or 4096 grid cells. A typical time step was 0.001.

Figure 5a shows the solution $A(x, t)$ for a run with $F_{max} = 1.25$, $T = 1000$, $w_b = 25$, and positive forcing $b_M = 0.03$. Here $\Delta_m < \Delta_{max} < \Delta_M$ from Figure 3. The passage of the forcing through the resonance regime excites undular bores upstream and downstream of the topography (centered at $x = 0$) similar to the constant $\Delta$ example in Figure 1. However the upstream waves are less regularly separated, reflecting the time variation of $\Delta$, and after the forcing peaks (at $t = 250$) the downstream bore begins to move upstream (scenario 2 above). Figure 5b shows the evolution for $F_{max} = 2$. Here $\Delta_{max} >$

$\Delta_M$ (scenario 3) so the forcing involves distinct acceleration and deceleration passages through the resonant region. This gives rise to a single upstream propagating solitary wave generated on the accelerating phase. A trailing packet evolves on the deceleration phase of the forcing from the release of the supercritical-like response over the topography.

The effect of changing $F_{max}$ is summarised Figure 6 where the solutions at the end of the forcing period, $A(x, t = T/2)$, are shown for several $0.5 \leq F_{max} \leq 2$. The other parameters are unchanged. For $F_{max} = 0.5$ and 0.75, $\Delta_{max} \lesssim \Delta_m$ and the upstream response is weak since the forcing at most just enters the resonant regime for a very brief period (scenario 1). Runs with $F_{max} = 1, 1.25$ and 1.5 ($\Delta_m < \Delta_{max} < \Delta_M$) all produce upstream and downstream bores (scenario 2). When $F_{max} \geq 1.75$, $\Delta_{max} \gtrsim \Delta_M$, the upstream response in particular reflects the two passages through resonance (scenario 3).

Solutions for negative forcing $b_M = -0.03$ and $F_{max} = 1.25$ and 2, with $T = 1000$ and $w_b = 25$ unchanged from above, are plotted in Figure 7. In both examples the negative forcing results in a downstream undular bore on the increasing phase of the barotropic flow that is released to move upstream as the tidal flow decreases for $t > 250$. Passage of the waves back over the forcing region leads to a more complicated and variable wave field upstream and over the topography than for positive forcing as anticipated from the constant forcing example of Figure 2. The effect of further variations in $F_{max}$, with the other parameters unchanged, on the solutions at $t = T/2$ are shown in Figure 8. Again, differences in the response reflect the magnitude of $\Delta_{max}$ in comparison to $\Delta_m$ and $\Delta_M$.

The effect of varying the topographic amplitude, $b_M$, for $F_{max} = 1.25$ ($\Delta_m < \Delta_{max} < \Delta_M$), $T = 1000$, and $w_b = 25$ is shown in Figure 9. In addition to the increase of topographic forcing magnitude, increases in $|b_M|$ also lead to increased duration of the barotropic forcing residing within the resonant band, hence larger and more numerous waves are generated.

The effect of forcing duration is further illustrated in Figures 10a and b that shows $A(x, T/2)$ for $T = 600$ and 1400, respectively. Here $b_M = 0.03$, $w_b = 25$, and $F_{max} = 0.5 - 2$. The same results for $b_M = -0.03$ are shown in Figure 11.

Figure 12 shows the effect of changing the topographic width scale from $w_b = 25$ to $w_b = 75$ on $A(x, T/2)$ for $b_M = 0.03$. Here $T = 1000$ and $F_{max} = 0.5 - 2$. This figure should be compared to Figure 6 where $w_b = 25$. The broader topography, hence weaker forcing through reduction of $s_x$, results in a weaker upstream and downstream bores for all $F_{max}$. However, for negative topographic forcing $b_M = -0.03$, Figure 13, the upstream propagating bore is eliminated, while the downstream response is increased in comparison to the narrower topography, $w_b = 25$, shown in Figure 8.

## 4. Generation of internal undular bores by tidal interaction with asymmetric topography

In order to compare this theory in more detail with the generation at actual sites, we note that in practice the forcing topography is often highly asymmetric. This is the case, for instance, with Stellwagen Bank (**??**), where the bank is much steeper on the shoreward side than on the ocean side. In Figure 14 we show some simulations representing ebb tide for Stellwagen Bank using a model topography of the same asymmetric shape as the actual topography. The simulations use both the fKdV model (Figure 14a) with a reduced topographic amplitude and a two-layer shallow water model (Figure 14b) with the full topography, both shown in the lower panels. The figure shows the interface evolution over the first half period of tidal forcing, and for an upper layer depth $h_1 = 12.75\, m = 0.15h$, where the total depth $h = 85\, m$, and reduced gravity $g' = 0.0196\, ms^{-2}$, giving $c_0 = 0.46\, ms^{-1}$. The plot is in dimensional units for direct comparison with observations.

Because KdV theory is formally limited to small amplitude topography, the solution in Figure 14a has the topographic amplitude reduced to $b_M = 12.75\,m$ (15% of the total depth) from the actual value of $b_M = 55\,m$, and $F_{max} = 1.5$. This topography and tidal amplitude place the forcing in scenario 2 since $\Delta_M = 0.54$. For comparison, Figure 14b shows the solution of the two-layer shallow water equations (non-dispersive) for the ebb forcing with the actual topography and a maximum upstream $F = 0.24$. This flow produces a maximum $F$ over the sill of about 1.5. The magnitude and direction of the tidal flow is indicated by the heavy lines in each case. Not surprisingly, the two figures show quantitatively different results and note that the shallow water simulations cannot produce the internal waves, but do show the steepening bores that leads to their formation. However, the qualitative features, especially the general shape and timing of the upstream-moving disturbances are in good agreement, suggesting that the fKdV model is capturing the essential features of the generation process on this ebb phase of the tide.

An equivalent pair of simulations for the Stellwagen Bank flood tide are shown in Figure 15. Again, there are quantitative differences between the fKdV and shallow water runs (e.g. the strong downstream jump is absent in the KdV simulation while the upstream waves are not present in the shallow water simulation), but the leading upstream disturbance front, at $x \approx 3 - 3.5\,km$, is captured in both. The effect of the topographic asymmetry leads to substantial changes in the response when compared to the ebb tide examples above.

Knight Inlet is another asymmetrical, tidally-forced sill (**??**). In Figure 16 we show fKdV and shallow water equation simulations for the flood tide. In these calculations the total water depth is taken to be $h = 100\,m$. This is less than the actual depth of approximately $350\,m$, but is about the depth of the downstream flow separation (**??**) on flood tide and thus is a reasonable approximation for the active total depth in a two-layered reduction. Again, the topographic shape replicates the steeper landward side of the sill, over which the water is $60\,m$ deep. For these simulations we use an upper layer depth $h_1 = 12\,m$ and reduced gravity $g' = 0.076\,ms^{-2}$, giving $c_0 = 0.90\,ms^{-1}$. Figure 16a shows the fKdV simulation for $b_M/h = 0.15$ and $F_{max} = 1.5$. The strengthening flood tide generates a wave packet that is trapped just upstream of the sill crest until the tide begins to slacken, after which the waves propagate upstream, in qualitative agreement with observations (**?**). In the companion two-layer shallow water simulation in Figure 16b the timing of the upstream disturbance mirrors the waves in the fKdV simulation, although the downstream hydraulic jump is both weaker and shorter lived in the fKdV model. Both simulations highlight the role of a subcritical zone between the upstream jump, or bore, and the hydraulic critical flow at the sill crest, in which the solitary waves develop (**?**). The Knight Inlet ebb tide fKdV and shallow water simulations are shown in Figure 17. Again the timing of the upstream propagating disturbances are qualitatively similar in both simulations. We note that in the Knight Inlet observations and numerical simulations, the strong flow deformation over the sill crest with local shear instability, mixing and possible formation of a three-layer flow structure, see **????** for instance, is not captured of course in either the fKdV model or in the two-layer simulations. Nevertheless, the formation of the upstream wave field is at least qualitatively captured suggesting that this is essentially determined by the passage of the Froude number through criticality as we have described in section 3 and as has been previously suggested by **?** and **?**.

## 5. Discussion

As discussed in the Introduction, our focus here is on the generation of ISW by barotropic tidal flow over localised topography for those cases when the tidal flow reaches criticality, or passes through criticality, at the peak stage of the tidal cycle. We are proposing that a suitable model for this scenario is the fKdV equation (2.13), expressed there in scaled canonical form. Unlike most previous studies of the fKdV equation, we allow the Froude number $F = 1 + \Delta$ to vary temporally over half a tidal cycle, from zero to a maximum value $F_{max}$. Then we have presented in section 3 several simulations for a symmetrical obstacle, where the main parameters varied are $F_{max}$, $b_M$ (the maximum obstacle height), $w_b$ the obstacle width, and the obstacle polarity. Although there are quantitative differences between these simulations, they all point towards the same conclusion. Nonlinear waves form near the obstacle as the tidal flow passes through criticality, and these are then released upstream in the form of undular bores as the tidal flow weakens towards zero. Because for many actual sites, the topography is not symmetric, in section 4 we presented some simulations for topography representing Stellwagen Bank and the Knight Inlet sill respectively, two heavily observed and modelled sites. Although there are some substantial differences with the results presented in section 3, the same basic conclusion can be reached, that is, large amplitude waves form near the obstacle at criticality and are released upstream as undular bores as the tidal flow weakens.

We infer that the fKdV model is a very useful resource for modelling and interpreting the formation of internal undular bores generated by tidal flow over localised topography. There are obvious limitations, such as the restriction to weakly nonlinear waves and small amplitude topography, so that intrinsically this model cannot describe the turbulence, and mixing produced at the obstacle sometimes seen in observations and in fully nonlinear numerical models. Also the fKdV model is restricted to a single vertical mode (assumed here to be mode one) and so cannot describe the possible generation of higher modes as occasionally observed. Further, like the KdV model, the fKdV model is unidirectional, and captures only the resonant wave. In practice flow interaction with topography will also generate waves propagating rapidly away from the topography, but these being non-resonant, can be expected to be usually quite small, and have been ignored here. Nonetheless, in spite of these limitations, the fKdV model is able to describe quite well the internal undular bores propagating upstream as the tidal flow slackens. Indeed, the trapping of large internal waves near the topography at criticality, and their release as the tidal flow slackens, would seem to be a very robust process, and essentially independent of the detailed flow structure over the topography itself.

## Acknowledgements

REFERENCES

AKYLAS, T., GRIMSHAW, R., CLARK, S. & TABAEI, A. 2007 Reflecting tidal wave beams and local generation of solitary waves in the ocean thermocline. *J. Fluid Mech.* **593**, 297–313.

ARMI, L. & FARMER, D. 2002 Stratified flow over topography: bifurcation fronts and transition to the uncontrolled state. *Proc. R. Soc.* **458A**, 513–538.

BUIJSMAN, M. C., KANARSKA, Y. & MCWILLIAMS, J. C. 2010 On the generation and evolution of nonlinear internal waves in the South China Sea. *J. Geophys. Res* **115**.

Cai, S., Long, X. & Gan, Z. 2002 A numerical study of the generation and propagation of internal solitary waves in the Luzon Strait. *Oceanologica Acta* **25**, 51–60.

Chen, G.-Y., Liu, C.-T., Wang, Y.-H. & Hsu, M.K. 2011 Interaction and generation of long-crested internal solitary waves in the South China Sea. *J. Geophys. Res.* **116**, C06013.

Cummins, P.F. & Armi, L. 2010 Upstream internal jumps in stratified sill flow: observations of formation. *J. Phys. Ocean.* **40**, 1419–1426.

Cummins, P., Vagle, S., Armi, L. & Farmer, D. 2003 Stratified flow over topography: upstream influence and generation of nonlinear internal waves. *Proc. R. Soc. Lond. A* **459**, 1467–1487.

Cummins, P. F., Armi, L. & Vagle, S. 2006 Upstream internal hydraulic jumps. *J. Phys. Ocean.* **36**, 753–769.

Duda, T. F., Lynch, J. F., Irish, J. D., Beardsley, R. C., Ramp, S. R., Chiu, C. S., Tang, T. Y. & Yang, Y. J. 2004 Internal tide and nonlinear internal wave behavior at the continental slope in the northern South China Sea. *IEEE J. Oceanic Eng* **29**, 1105–1130.

Farmer, D. M. & Armi, L. 1999a The generation and trapping of solitary waves over topography. *Science* **283**, 188–190.

Farmer, D. M. & Armi, L. 1999b Stratified flow over topography: the role of small scale entrainment and mixing in flow establishment. *Proc. Roy. Soc.* **455A**, 3221–3258.

Farmer, D. M. & Armi, L. 2001 Stratified flow over topography: models versus observations. *Proc. Roy. Soc.* **457A**, 267–280.

Farmer, D. M. & Smith, J. D 1980 Tidal interaction of stratified flow with a sill in Knight Inlet. *Deep-Sea Res.* **27A**, 239–254.

Gerkema, T. 2001 Internal and interfacial tides: Beam scattering and local generation of solitary waves. *J. Mar. Res.* **59**, 227–255.

Grimshaw, R. 2010 Transcritical flow past an obstacle. *ANZIAM J.* **52**, 1–25.

Grimshaw, R., Pelinovsky, E. & Talipova, T. 2007 Modeling internal solitary waves in the coastal ocean. *Surveys in Geophysics* **28**, 273–298.

Grimshaw, R., Pelinovsky, E., Talipova, T. & Kurkina, A. 2010 Internal solitary waves: propagation, deformation and disintegration. *Nonlinear Processes in Geophysics* **17**, 633–649.

Grimshaw, R. H. J. & Smyth, N. F 1986 Resonant flow of a stratified fluid over topography. *J. Fluid Mech.* **169**, 429–464.

Guo, C., Chen, C., Vlasenko, V. I. & Stashchuk, N. 2011 Numerical investigation of internal solitary waves from the Luzon strait: generation process, mechanism and three-dimensional effects. *Ocean Modelling* **38**, 203–216.

Helfrich, K. R. & Melville, W. K. 2006 Long nonlinear internal waves. *Ann. Rev. Fluid Mech.* **38**, 395–425.

Hibiya, T. 1988 The generation of internal waves by tidal flow over Stellwagen Bank. *J. Geophys. Res.* **93**, 533–542.

Holloway, P., Pelinovsky, E. & Talipova, T. 2001 Internal tide transformation and oceanic internal solitary waves. In *Environmental Stratified Flows* (ed. R. Grimshaw), pp. 31–60. Boston: Kluwer.

Lai, Z., Chen, C., Cowles, G. W. & Beardsley, R. C. 2010 A nonhydrostatic version of FVCOM: 2. Mechanistic study of tidally generated nonlinear internal waves in Massachusetts Bay. *J. Geophys. Res.* **115**, C12049.

Lee, C.-Y. & Beardsley, R. C. 1974 The generation of long nonlinear internal waves in weakly stratified shear flows. *J. Geophys. Res.* **79**, 453–462.

Li, Q. & Farmer, D. M. 2011 The generation and evolution of nonlinear internal waves in the deep basin of the South China Sea. *J. Phys. Ocean.* **41**, 1345–1363.

Liu, A. K., Chang, Y. S., Hsu, M. K. & Liang, N. K. 1998 Evolution of nonlinear internal waves in the east and South China Seas. *J. Geophys, Res* **103**, 7995–8008.

Liu, A. K., Ramp, S. R., Zhao, Y. & Tswen Yung Tang, T. Y. 2004 A case study of internal solitary wave propagation during ASIAEX 2001. *IEEE J. Oceanic Eng* **29**, 1144–1156.

Liu, Ch-T, Pinkel, R., Klymak, J., Hsu, M. K., Chen, H. W. & C. Villanoy, C 2006 Nonlinear internal waves from the Luzon strait. *EOS* **87**, 449.

MAXWORTHY, T. 1979 A note on the internal solitary waves produced by tidal flow over a three-dimensional ridge. *J. Geophys. Res.* **84**, 338–346.

MELVILLE, W. K. & HELFRICH, K. R. 1987 Transcritical 2-layer flow over topography. *J. Fluid Mech.* **178**, 31–52.

ORR, M. H. & MIGNEREY, P. C. 2003 Nonlinear internal waves in the South China Sea: Observation of the conversion of depression internal waves to elevation internal waves. *J. Geophys. Res* **108(C3)**, 3064.

RAMP, S. R., TANG, T. Y., DUDA, T. F., LYNCH, J. F., LIU, A. K., CHIU, C. S., BAHR, F. L., KIM, H. R. & YANG, Y. J. 2004 Internal solitons in the northeastern South China Sea. Part i: sources and deep water propagation. *IEEE J. Oceanic Eng.* **29**, 1157–1181.

REDEKOPP, L. G. & YOU, Z. 1995 Passage through resonance for the forced korteweg-de vries equation. *Phys. Review Lett.* **74**, 5158–6161.

SCOTTI, A., BEARDSLEY, R. C. & BUTMAN, B. 2007 Generation and propagation of nonlinear internal waves in Massachusetts Bay. *J. Geophys. Res.* **112**, C10001.

SCOTTI, A., BEARDSLEY, R. C., BUTMAN, B. & PINEDA, J. 2008 Shoaling of nonlinear internal waves in Massachusetts Bay. *J. Geophys. Res* **113**, C08031.

STASHCHUK, N. & VLASENKO, V. I. 2007 Numerical modelling of stratified tidal flow over a fjord sill. *Ocean Dynamics* **57**, 325–338.

STASTNA, M. & PELTIER, W. R. 2004 Upstream-propagating solitary waves and forced internal-wave breaking in stratified flow over a sill. *Proc. Roy. Soc. Lond.* **A460**, 3159–3190.

STASTNA, M. & PELTIER, W. R. 2005 On the resonant generation of large-amplitude internal solitary and solitary-like waves. *J. Fluid Mech.* **543**, 267–292.

VLASENKO, V. I., GUO, C. & STASHCHUK, N. 2012 On the mechanism of A-type and B-type internal solitary wave generation in the northern South China Sea. *Deep-Sea Res. I* **69**, 100–112.

VLASENKO, V. I., STASHCHUK, N., GUO, C. & X. CHEN, X 2010 Multimodal structure of baroclinic tides in the South China Sea. *Nonlinear Processes in Geophysics* **17**, 529–543.

WARN-VARNAS, A., HAWKINS, J., LAMB, K. G., PIACSEK, S., CHIN-BING, S., KING, D. & BURGOS., G 2010 Solitary wave generation dynamics at Luzon Strait. *Ocean Modelling* **31**, 9–27.

WILLIAMSON, J. H. 1980 Low-storage Runge-Kutta schemes. *J. Comp. Phys.* **35**, 48–56.

ZHAO, Z. & ALFORD, M. H. 2006 Source and propagation of internal solitary waves in the northeastern South China Sea. *J. Geophys. Res* **111**, C11012.
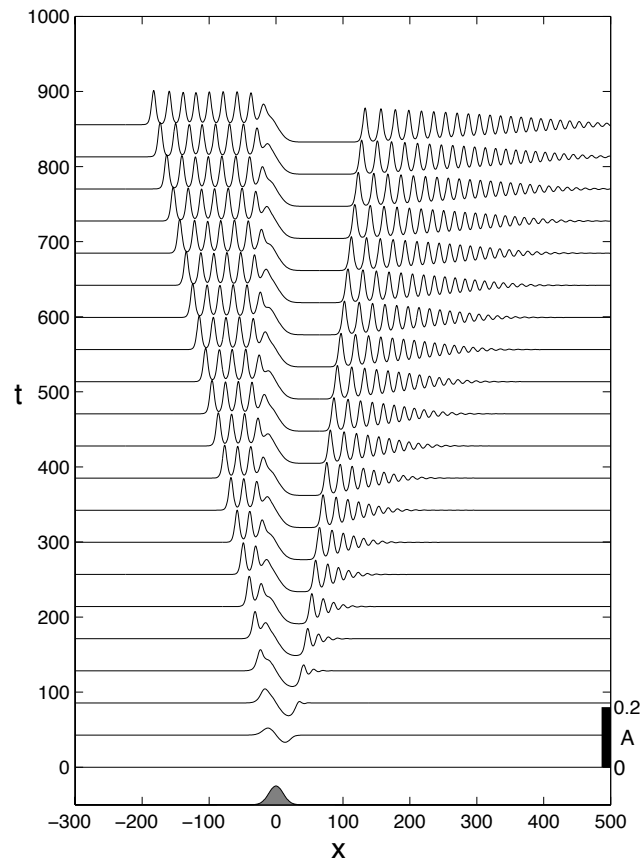
FIGURE 1. Numerical solution of the fKdV equation (2.13) for a localized obstacle, with $b_M = 0.01$ and $\Delta = 0$. The location and shape of the topography (arbitrary amplitude) is shown at the bottom of the plot.
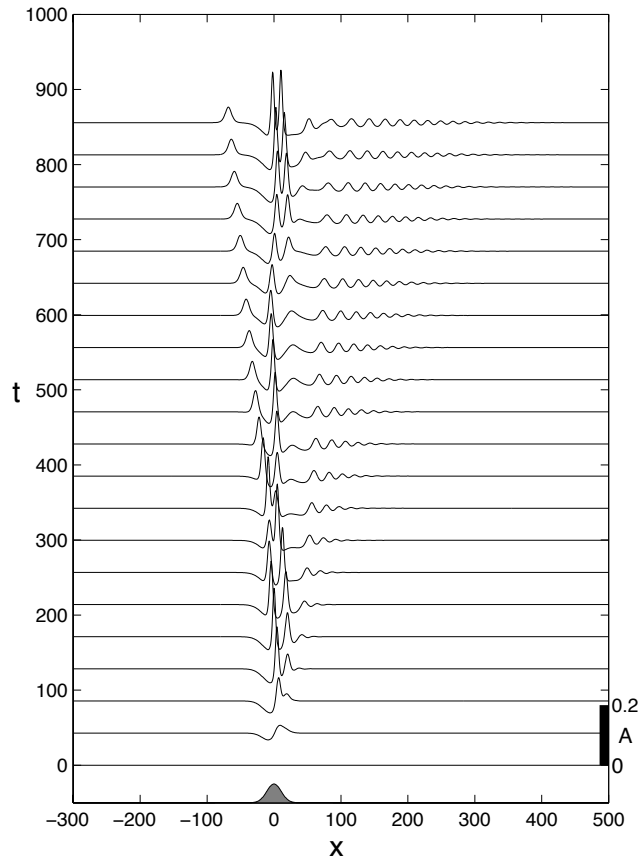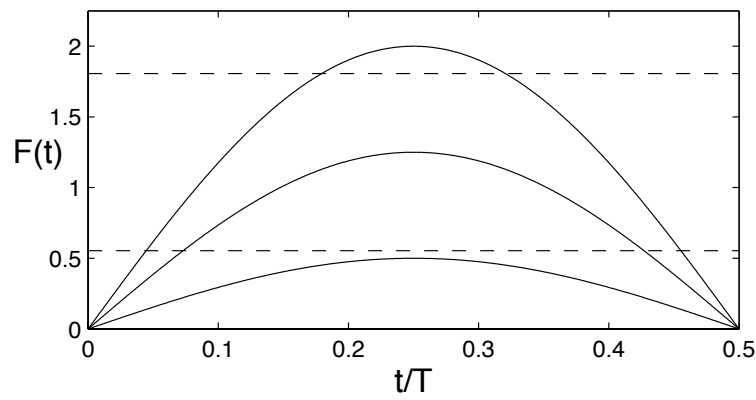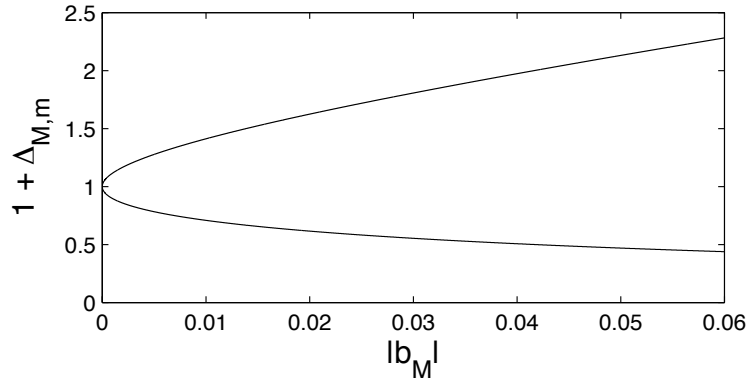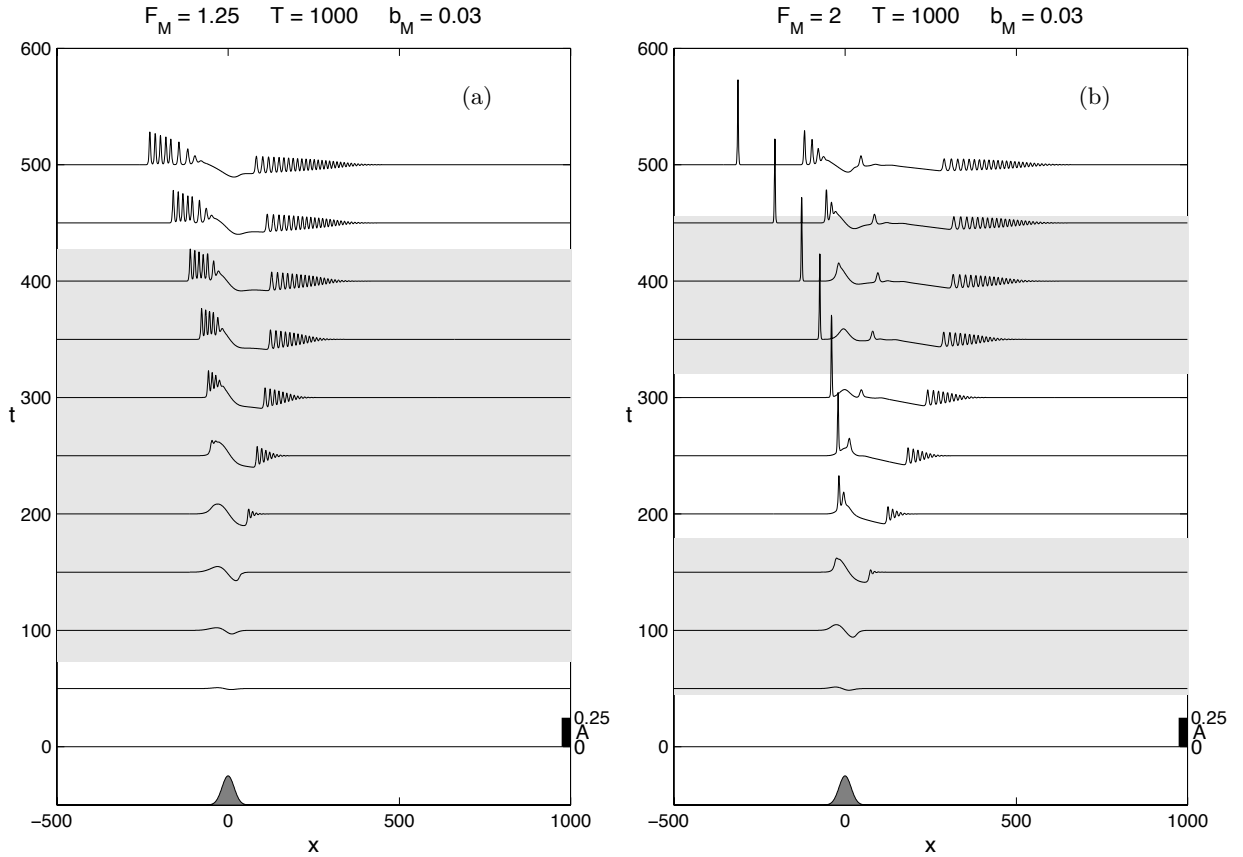
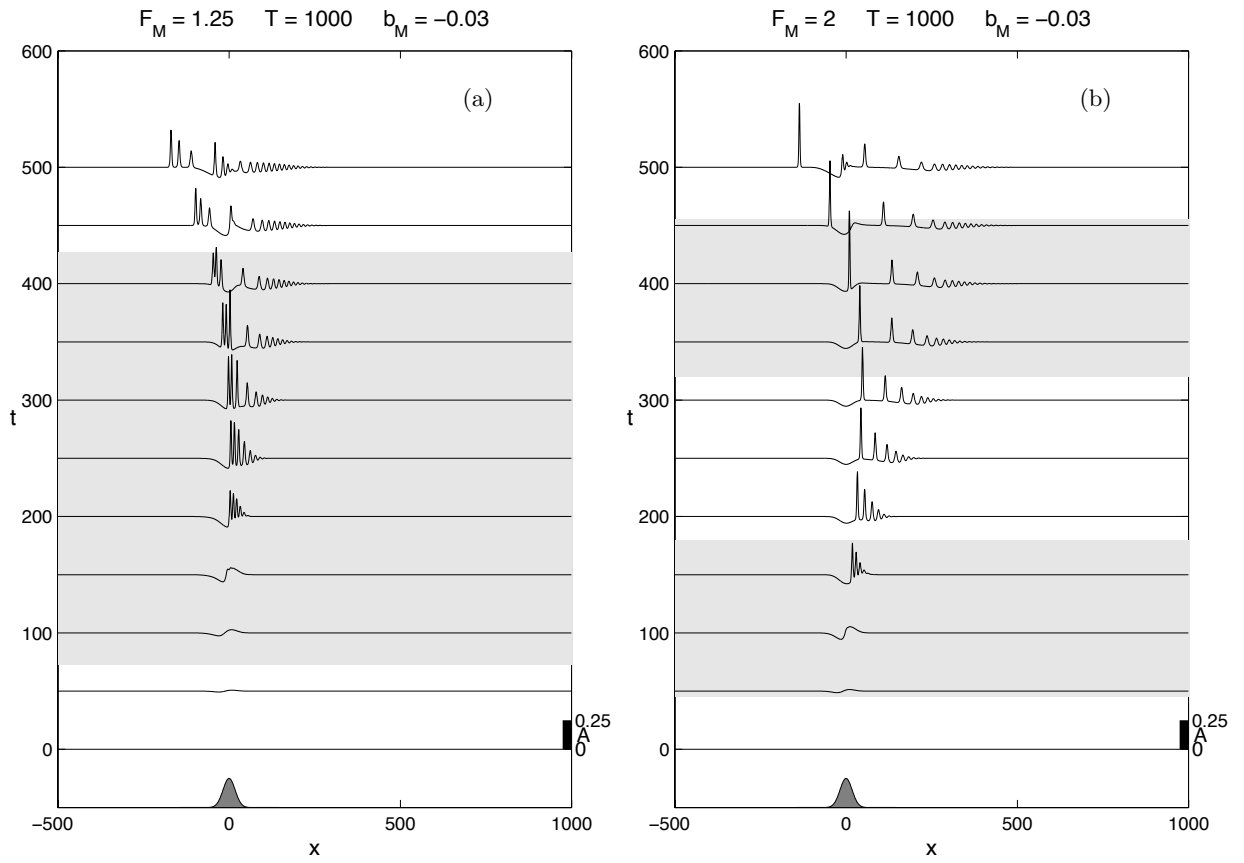FIGURE 2. The same Figure 1 except $b_M = -0.01$.



FIGURE 3. $F(t)$ from (3.1) for $F_{max} = 0.5$, 1.25, and 2. Here $T = 2\pi/\omega$. The dashed lines indicate the resonant regime from (2.15) for $|b_M| = 0.03$.

FIGURE 4. The resonant band limits $1 + \Delta_{M,m}$ from (2.15).



FIGURE 5. a) Solution of (2.13) for $(b_M, T, w_b) = (0.03, 1000, 25)$ with $F_{max} = 1.25$. b) Same except $F_{max} = 2$. The location and shape of the topography (arbitrary amplitude) is shown at the bottom of the plot. The light gray shading indicates the time when the forcing is in the critical region, $\Delta_m < F(t) - 1 < \Delta_M$, from (2.15) and (3.1).
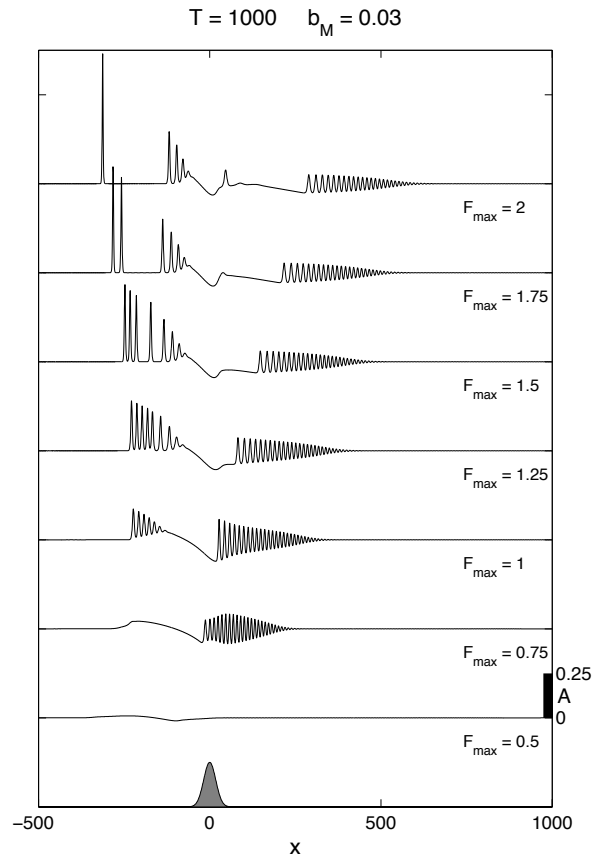
FIGURE 6. $A(x, T/2)$ for $(b_M, T, w_b) = (0.03, 1000, 25)$ and $F_{max}$ as indicated. The location and shape of the topography (arbitrary amplitude) is shown at the bottom of the plot.

FIGURE 7. The same as Figure 5 except $b_M = -0.03$. a) $F_{max} = 1.25$. b) $F_{max} = 2$.

T = 1000    $b_M$ = −0.03
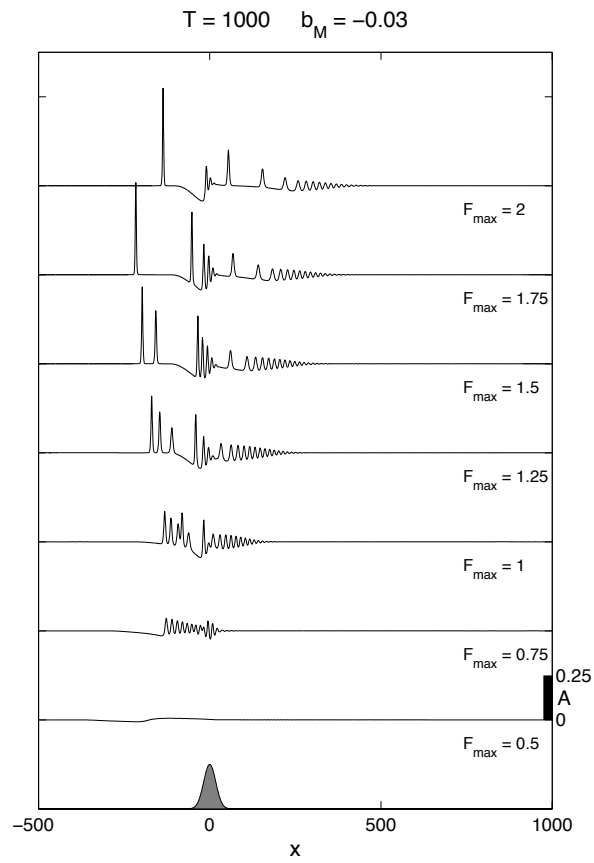


FIGURE 8. $A(x, T/2)$ for $(b_M, T, w_b) = (-0.03, 1000, 25)$ and $F_{max}$ as indicated.
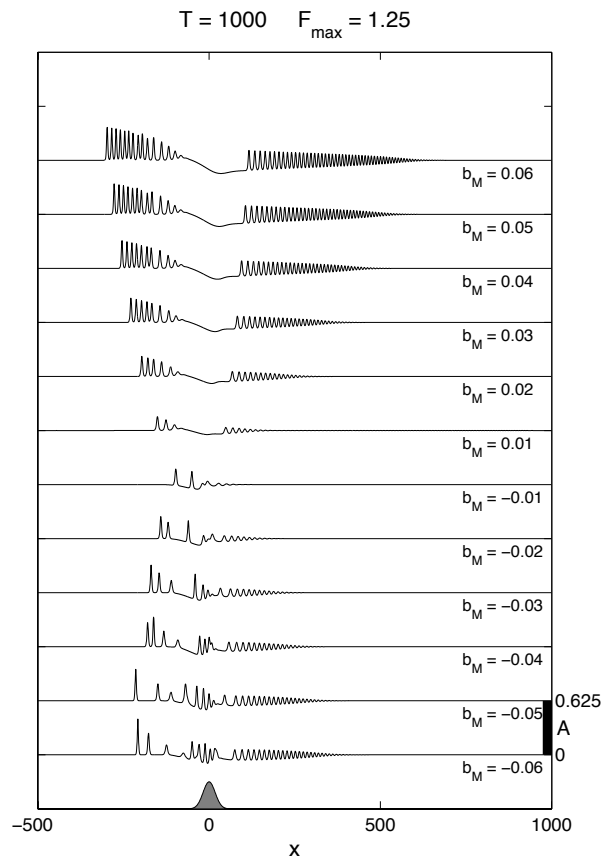
FIGURE 9. $A(x, T/2)$ for $(F_{max}, T, w_b) = (1.25, 1000, 25)$ and $b_M$ as indicated.
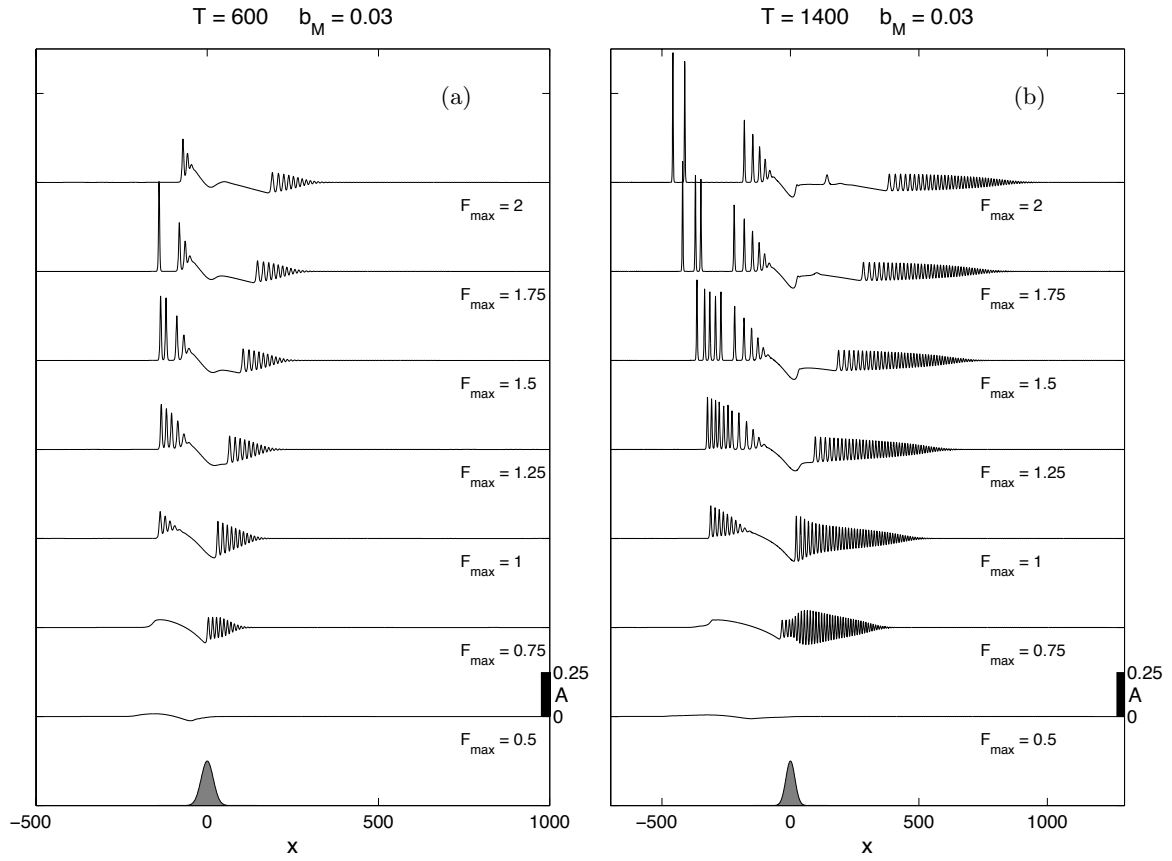
FIGURE 10. a) $A(x, T/2)$ for $(b_M, w_b) = (0.03, 25)$, $F_{max}$ as indicated, and $T = 600$. b) Same except $T = 1400$.
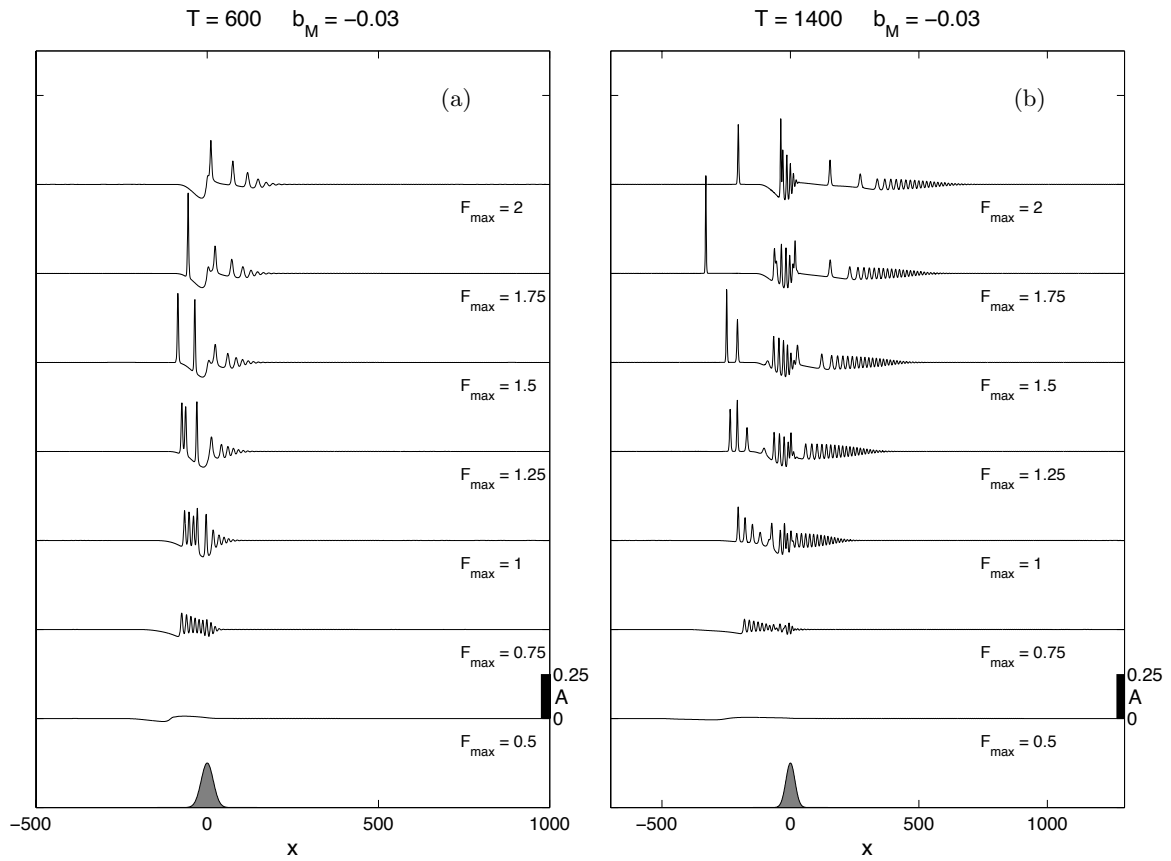
FIGURE 11. a) $A(x, T/2)$ for $(b_M, w_b) = (-0.03, 25)$, $F_{max}$ as indicated, and $T = 600$. b) Same except $T = 1400$.
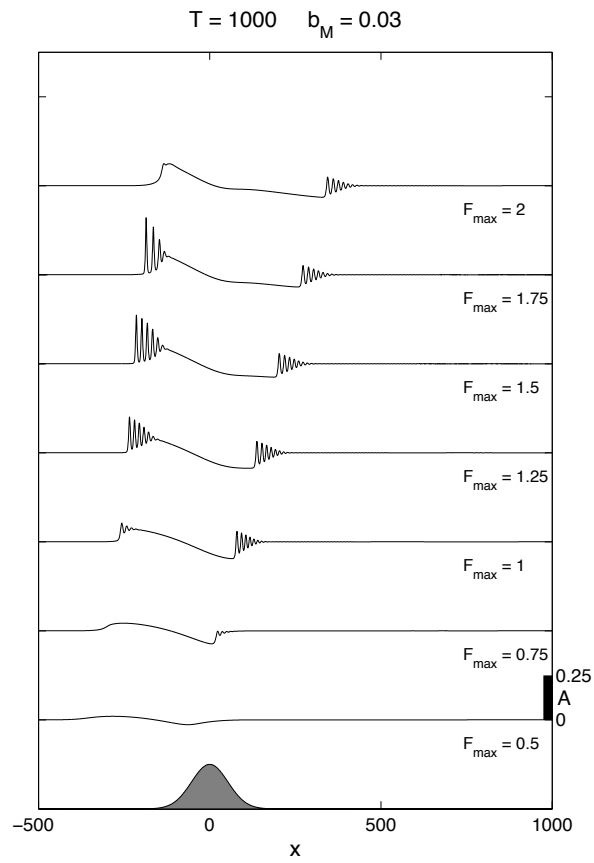
FIGURE 12. $A(x, T/2)$ for $w_b = 75$, $T = 1000$ and $b_M = 0.03$ with $F_{max}$ as indicated.

*R. Grimshaw and K. R. Helfrich*
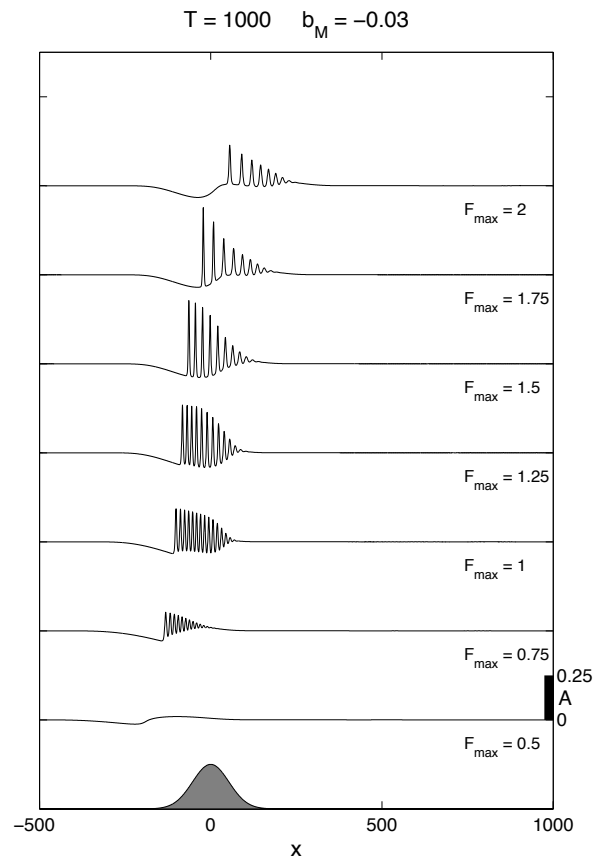


FIGURE 13. $A(x, T/2)$ for $w_b = 75$, $T = 1000$ and $b_M = -0.03$ with $F_{max}$ as indicated.
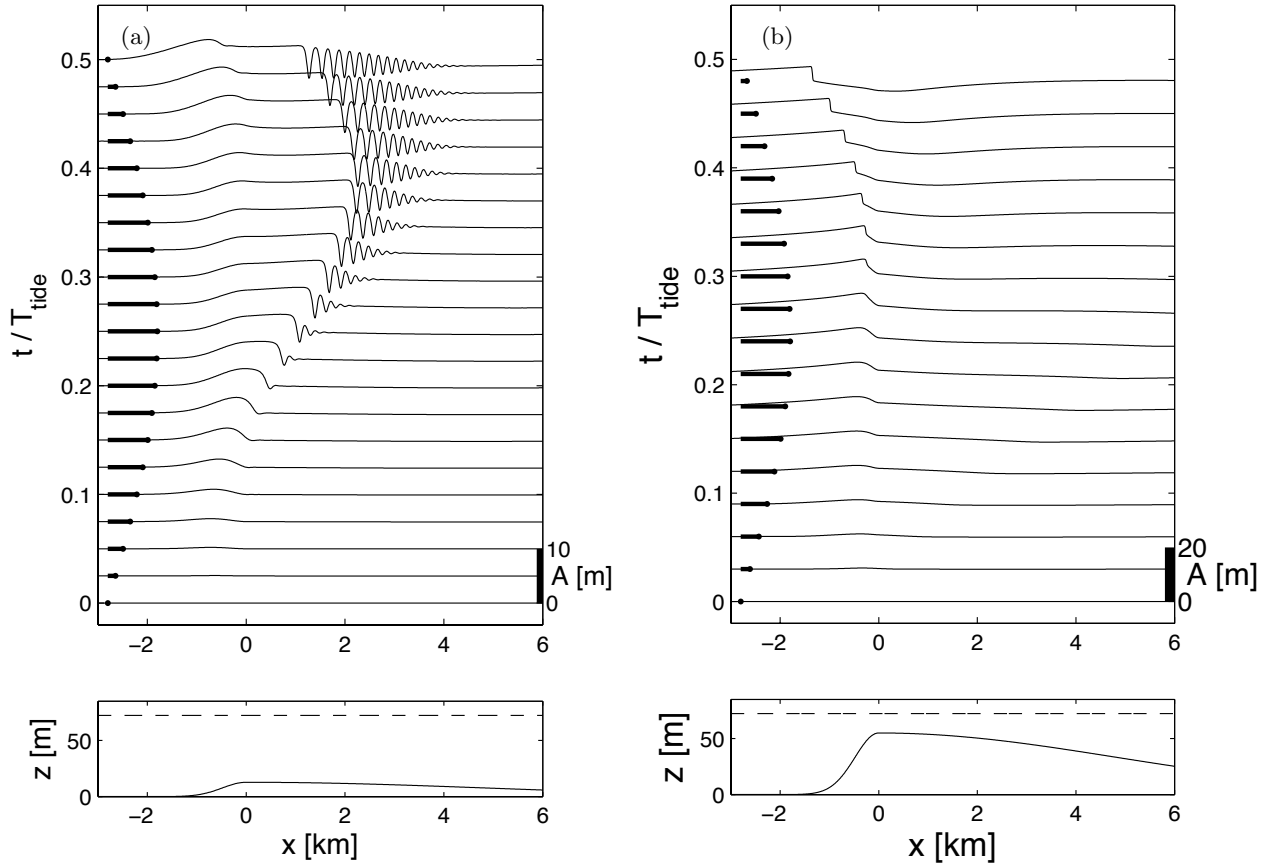
FIGURE 14. a) Numerical solution of the fKdV equation (2.13) for a representation of Stellwagen Bank for an ebb tide with $b_M/h = 0.15$, $h = 85\,m$ and $F_{max} = 1.5$. b) Numerical solution of the two-layer shallow water equations for an ebb tide with the actual topography, $b_M/h = 0.65$, and an maximum upstream $F = 0.24$. The lower panels show the topography and the resting interface position. The upper panels show the interface displacement through the tidal forcing. The magnitude and direction of the barotropic flow are indicated by the heavy lines.
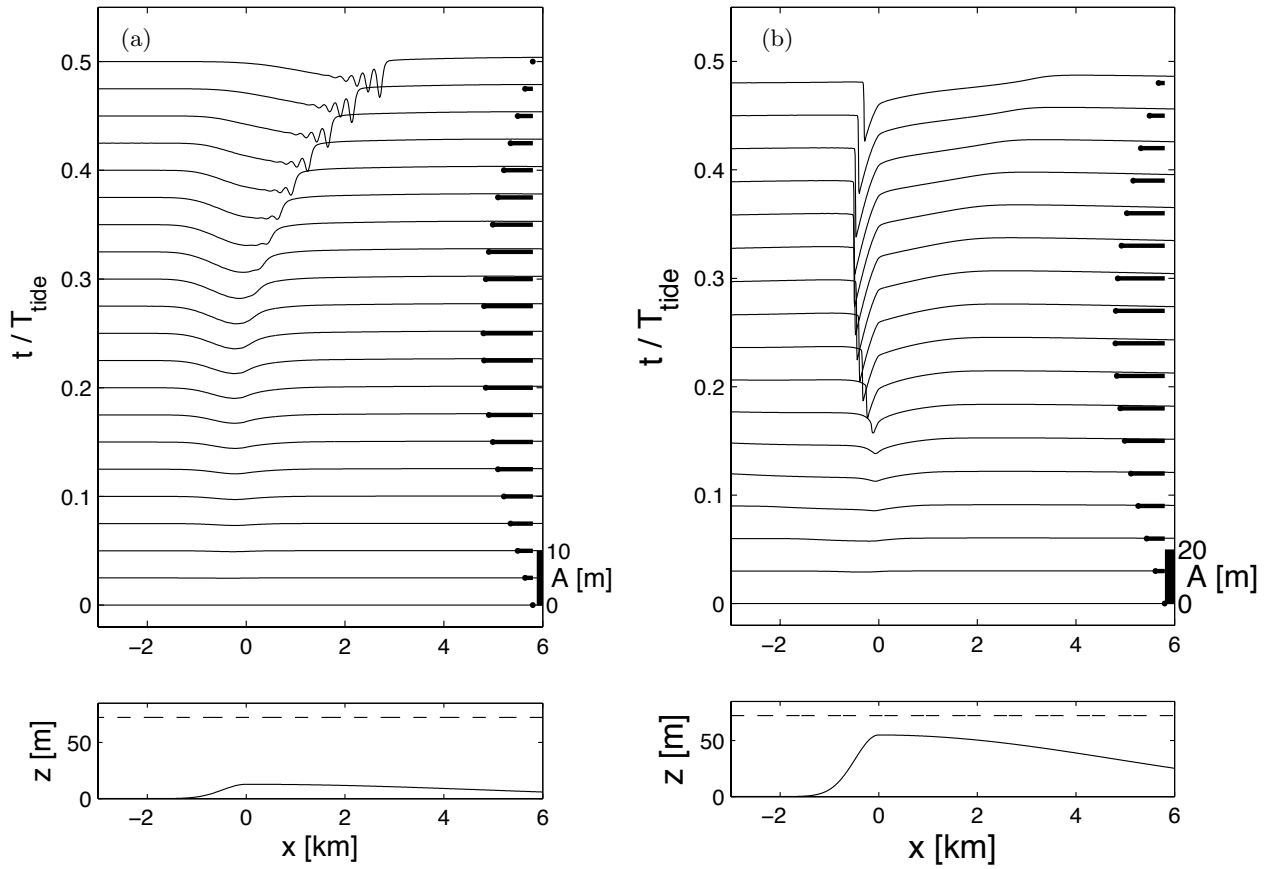
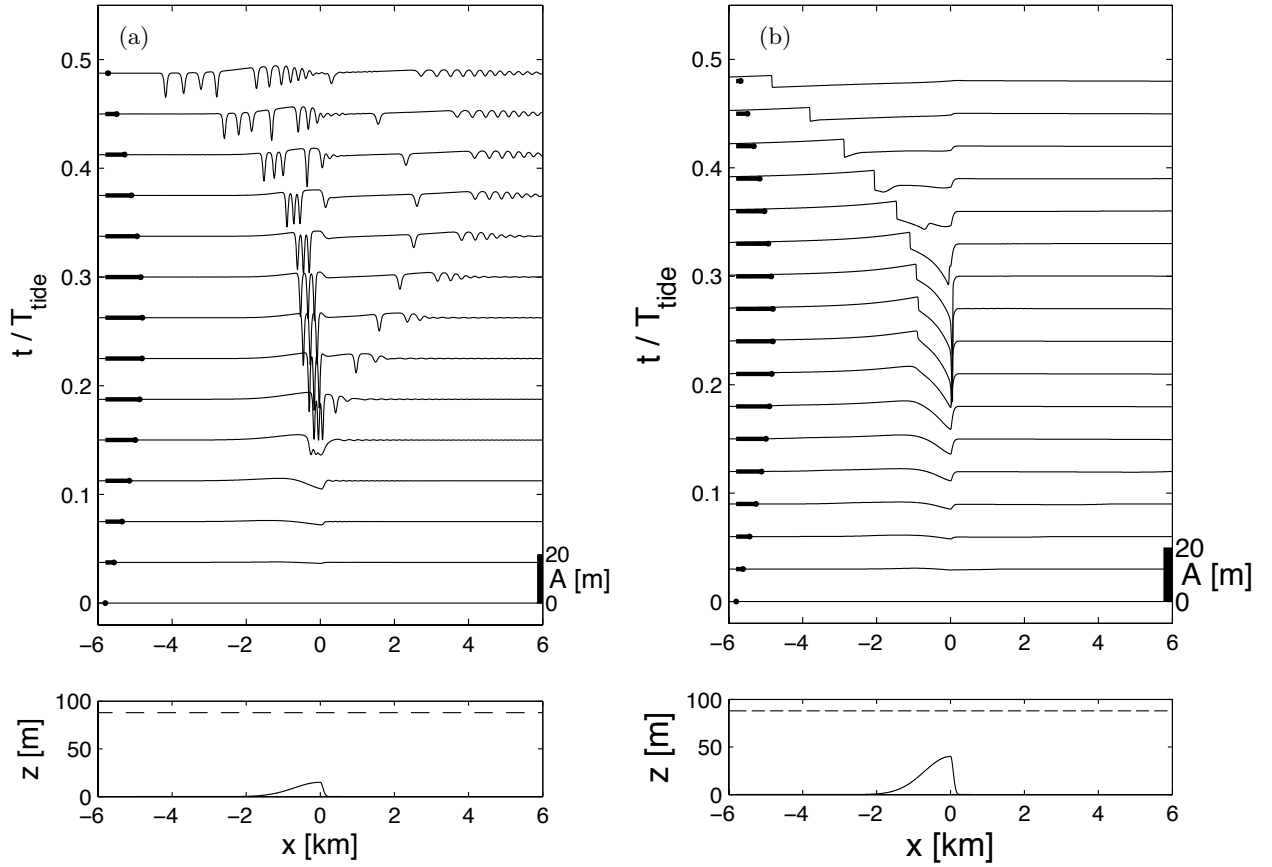FIGURE 15. The same as Figure 14, but now for the flood tide.

FIGURE 16. a) Numerical solution of the fKdV equation (2.13) for a representation of Knight Inlet sill for a flood tide with $b_M/h = 0.15$, $h = 100\,m$ and $F_{max} = 1.5$. b) Numerical solution of the two-layer shallow water equations for an ebb tide with the full topography, $b_M/h = 0.4$, and an maximum upstream $F = 0.66$. The lower panels show the topography and the resting interface position. The upper panels show the interface displacement through the tidal forcing. The magnitude and direction of the barotropic flow are indicated by the heavy lines.
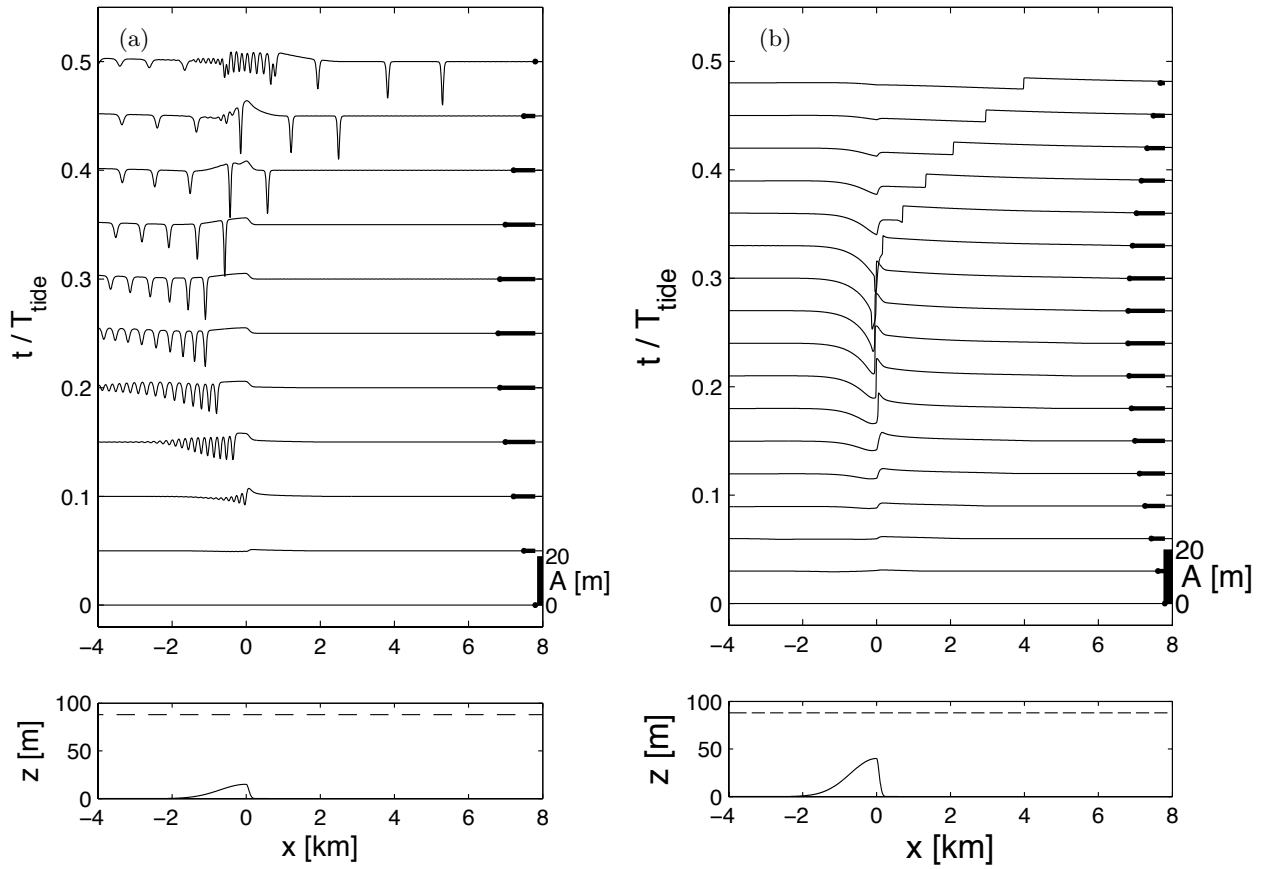
FIGURE 17. The same as Figure 16, but now for the ebb tide.